

# Comparison of RFI Mitigation Strategies for Dispersed Pulse Detection

John Hogden<sup>1</sup> and Scott Vander Wiel<sup>1</sup> and Geoffrey C. Bower<sup>2</sup> and Sarah Michalak<sup>1</sup> and Andrew Siemion<sup>2</sup> and Daniel Werthimer<sup>2</sup>

## Abstract

Impulsive radio-frequency signals from astronomical sources are dispersed by the frequency dependent index of refraction of the interstellar media and so appear as chirped signals when they reach earth. Searches for dispersed impulses have been limited by false detections due to radio frequency interference (RFI) and, in some cases, artifacts of the instrumentation. Many authors have discussed techniques to excise or mitigate RFI in searches for fast transients, but comparisons between different approaches are lacking. This work develops RFI mitigation techniques for use in searches for dispersed pulses, employing data recorded in a “Fly’s Eye” mode of the Allen Telescope Array as a test case. We gauge the performance of several RFI mitigation techniques by adding dispersed signals to data containing RFI and comparing false alarm rates at the observed signal-to-noise ratios of the added signals. We find that Huber filtering is most effective at removing broadband interferers, while frequency centering is most effective at removing narrow frequency interferers. Neither of these methods is effective over a broad range of interferers. A method that combines Huber filtering and adaptive interference cancellation provides the lowest number of false positives over the interferers considered here. The methods developed here have application to other searches for dispersed pulses in incoherent spectra, especially those involving multiple beam systems.

<sup>1</sup>Los Alamos National Laboratory, Los Alamos, New Mexico, USA

<sup>2</sup>University of California, Berkeley - Department of Astronomy, Berkeley, California, USA

## 1. Background

Variable radio sources probe extreme physical conditions in the Universe: the sparks that emerge from high energy density regions around compact objects such as black holes, neutron stars, and magnetized stars, and the glowing embers that appear in the afterglow of relativistic explosions (e.g., Cordes et al. 2004). Fast transients are distinguished from slow transients both physically and through the technology required to detect them. Typically, fast transients originate from coherent emission processes and have time scales of  $\sim 1$  second or less. Examples include pulsar emission, cyclotron masers, and electrostatic discharges. The short timescale of fast transients drives a technological solution for discovery: typically these sources are found and characterized through the analysis of high time resolution incoherent spectra obtained from single dish telescope observations.

Pulsars are of great scientific interest. These rotating neutron stars are the most accurate clocks in the Universe and may be used for unique tests of general relativity, the nuclear equation of state, and the processes of star formation and death (Kramer & Stairs 2008). Pulsars produce both continuous pulse trains, that are discovered through periodicity searches, as well as bright individual pulses, such as Crab giant pulses (Hankins et al. 2003; Cordes et al. 2004; Bhat et al. 2008) and those from rotating radio transients (RRATs McLaughlin et al. 2006).

Of significant interest is the recent discovery of a very bright single pulse, only milliseconds in duration (Lorimer et al. 2007). The pulse is inferred to originate outside of the Galaxy, possibly at a distance of a billion light years, implying a source of enormous energy density. Subsequent investigations have supported both cosmological (Keane et al. 2011) and terrestrial origins (Burke-Spolaor et al. 2011) for similar events. The so-called “Lorimer burst” is controversial, however, because of the possibility that the event is due to man-made radio signals or radio frequency interference (RFI).

RFI presents a significant limitation on the ability to detect and characterize pulsed emission. Man-made radio signals occur throughout the radio spectrum, are variable in time and frequency, and can be strong enough to be detected in the far-out sidelobes of the antenna primary beam response (Ellingson 2005). Examples of RFI are satellite transmissions, aircraft communications, radar, TV, radio, cell phone, and other point-to-point communication systems. In the time domain, RFI may be steady, erratic, repeating, or isolated and may have a broad range of timescales. In the frequency domain, RFI may be narrowband, broadband, spread spectrum, regularly structured, or irregularly structured. Hybrids of these time- and frequency-modes, such as swept-frequency signals, are common.

The dispersion of celestial pulses imposed by propagation through the ionized interstellar

medium provides a unique signature that is a powerful discriminant against RFI (e.g., Deneva et al. 2009). Nevertheless, detection methods can be improved through the use of algorithms that excise or mitigate RFI. Standard searching for pulsed emission removes RFI through excision of frequency channels and time segments that are suspected to contain RFI based on amplitude thresholding (e.g., the PRESTO software, Ransom 2001).

In general, a wide range of methods for identification and mitigation of RFI has been considered (most recently reviewed by Baan 2010), including post-correlation matrix projection methods (Leshem et al. 2000; Kocz et al. 2010), blanking (e.g., Deneva et al. 2009) and coherent subtraction (Ellingson & Hampson 2003). Recently, kurtosis in the distribution of voltage measurements has been employed for RFI detection for single dish data (e.g., Nita & Gary 2010). Each technique has strengths and weaknesses relative to different types of RFI. Post-correlation methods are appropriate to interferometric visibility data. Blanking is most often applied to impulsive time-domain RFI. RFI rejection is carried out both in post-processing and in real-time through dedicated digital instrumentation (e.g., Weber et al. 1997).

Of particular applicability to pulse detection from single dish systems is adaptive interference cancellation (AIC, Widrow & Stearns 1985) in which a small reference antenna is employed for detection of a voltage stream that contains the RFI but not the astronomical signal. Cross-correlation of the two voltage streams can generate weights that are used to subtract the reference stream from the astronomy stream. The AIC method was first used for RFI excision in radio astronomy by Barnbaum & Bradley (1998) and has been applied or is being considered for many new radio telescopes (Kesteven et al. 2005; Li et al. 2008). Bower (2005) discusses the theory of using AIC with telescope arrays. Laboratory and field tests have demonstrated that the technique can effectively cancel interferers (e.g., Bower 2001). AIC has an advantage over other techniques, in that it makes no assumption about the frequency- or time-domain characteristics of the RFI.

Searches for dispersed pulses should robustly cope with a wide variety of interference, producing low false detection rates with little impact on sensitivity to true astronomical impulses. Our goal is to develop and compare different RFI mitigation techniques to help determine which are most useful. In particular, we are interested in exploring the efficacy of different methods through an evaluation based on actual RFI observed in incoherent spectra. Theoretical estimates of algorithm performance can be valuable, but it is almost always the case for RFI mitigation that the variety of RFI phenomena imply that no particular method is ideal or will meet its theoretical sensitivity under all (or any) circumstances.

In Section 2, we describe the incoherent spectra data obtained in the ATA Fly’s Eye experiment. In Section 3, we provide a compact mathematical formalism for the set of RFI

filtering techniques that we are exploring in this paper. We do this with the goal of providing a clear statement of the content of the techniques explored; many of these techniques have been put to use by other researchers. Since different methods of signal detection may give different false alarm results when paired with the same filtering method, in Section 4 we describe the chirp detection technique we used in our study of various RFI filters. Section 5 describes how we tested combinations of RFI filters with a chirp detection algorithm on various forms of RFI. Results of combining the mitigation techniques in various ways are shown in Section 6. Conclusions are in Section 7.

Our results should guide further research in RFI mitigation for searches using incoherent spectra. In particular, the use of multi-beam systems such as those at Parkes and Arecibo can directly make use of the techniques described here. Future instruments such as ASKAP may also make use of incoherent spectra for detection of fast transients (Macquart et al. 2010), and these methods would be readily applicable there as well.

## 2. Fly’s Eye Data

We have carried out an observing campaign using the Allen Telescope Array (ATA, Welch et al. 2009) that uses a novel observing technique, described below, to achieve high sensitivity to very bright, very rare, short-duration transients. The Fly’s Eye survey was carried out to detect events similar to the Lorimer burst. The ATA consists of 42 6.1-m dishes, each equipped with a log-periodic feed that is instantaneously sensitive to radio frequencies from 0.5 to 11.2 GHz.

Data from the ATA were captured in a fast spectrum fly’s eye mode (Siemion et al. 2010, 2011) in which each antenna can be pointed to a different patch of the sky in order to cover a large area at the expense of interferometric information and thus spatial resolution. In this mode, the digitally sampled waveform from each antenna in the array is mixed to baseband and converted to the frequency domain (channelized) via Fourier techniques; in this case, a 128 channel streaming polyphase filterbank is computed over 512-sample windows. Successive channelized windows are accumulated as a power spectrum and the cumulative spectra are written rapidly to disk. We recorded 128-channel accumulated power spectra at a continuous rate of 1600 spectra per second for each of 44 antennas using 8 bits of precision. Data were obtained at RF frequencies that spanned from 1325 to 1535 MHz. Accumulated power spectra are known as incoherent data because the detection process removes phase information from the signal.

Figure 1 shows two examples of dispersed pulses from the Crab pulsar as observed in

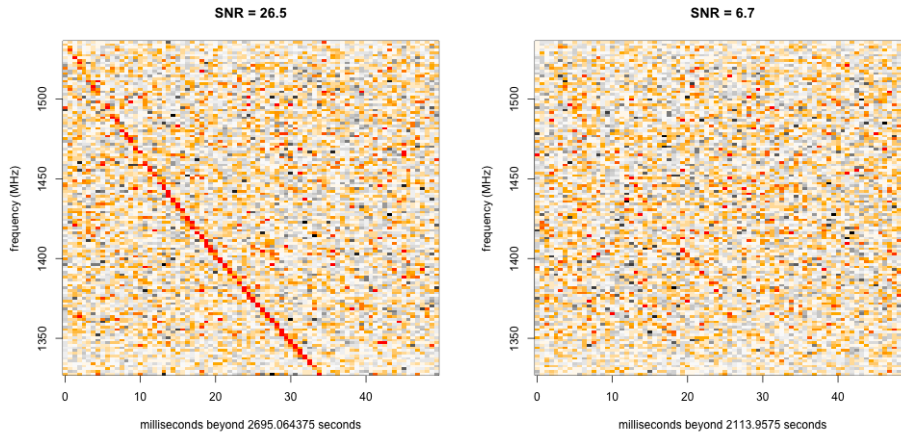


Fig. 1.— Two detections of giant pulses from the Crab pulsar. The left plot shows the brightest pulse detected in one hour of observation using 44 input streams. The right plot shows the 13th brightest pulse. Intensity is represented by the pixel colors scale from red to black, with red representing the highest intensity.

ATA fast spectrum data. The left-hand plot shows a strong detection, with signal to noise (SNR) of 26.5, while the right-hand plot shows an event with SNR of 6.7. The Crab pulsar has a dispersion measure of  $DM \sim 57 \text{pc}/\text{cm}^3$ , which translates to a 35 ms delay between the highest and lowest frequency channels in the observed band. The curves follow the expected quadratic dependence of the cold plasma dispersion relation.

Figure 2 shows examples of RFI from the Fly’s Eye data. Each image is a spectrogram of data collected on a single antenna at the ATA. The band pass response of the antenna (a smooth function of frequency) has been subtracted from the spectra before plotting in order to highlight the structure of the interference. In the left-hand image, the vertical stripe at 20 ms is an RFI impulse that affects all frequency channels, whereas the horizontal segment beginning at 310 ms is a transient RFI event at a single frequency, 1380 MHz. The right-hand image shows two prominent features; a 60 cycle per second pattern synchronized over all frequencies and a 20 ms period of time, ending at 300 ms, in which all frequencies have lower power than usual. Several of the frequency channels in either image have power levels that are sharply higher than adjacent channels and subtle horizontal striations indicate that power does not always vary smoothly with frequency. The goal of this work is to mitigate the effects of these and other types of RFI in anomaly detection in Fly’s Eye data.

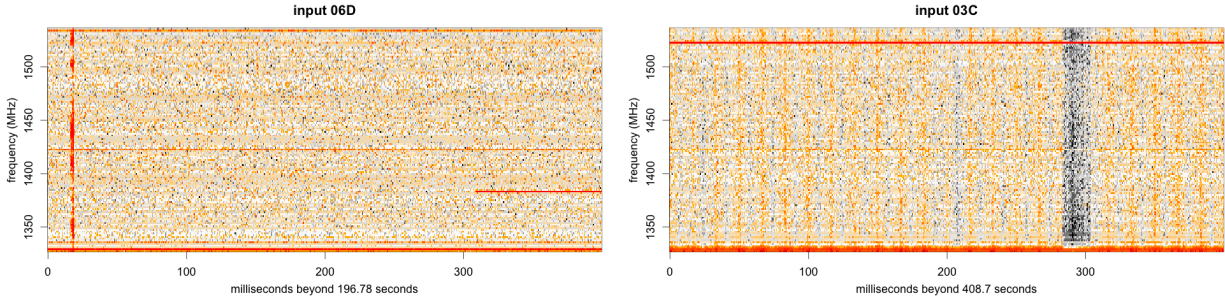


Fig. 2.— Examples of RFI in two spectrograms. The left plot has an impulse across the full frequency range at 20 ms and a transient increase at 1380 MHz beginning at 310 ms. The right plot has a 60 cycle per second pattern across the frequency range and a 20 ms wide dark vertical feature ending at 300 ms. Several horizontal stripes at various shades of red are frequency channels with more power than their neighbors. A stripe at 1425 MHz appears in both plots and indicates a persistently higher energy at that frequency.

### 3. RFI Mitigation Filters

Five RFI filtering methods are discussed below: *time centering* removes means for each time sample in a spectrogram whereas *frequency centering* removes means for each frequency; *energy clipping* normalizes spectra whose total energy exceeds a threshold; *Huber normalization* is a nonlinear high-pass normalizing filter in the time direction that clips outlying pixels to  $L$  standard deviations; and *adaptive interference cancellation* (AIC) cleans the signal from a target antenna by removing any correlated portion that it shares with a set of reference antennas. Each filter operates on a *spectrogram* (sequence of spectra). In the case of AIC, a set of reference spectrograms is also required. Filters are sometimes used in series, so each input spectrogram may have already been modified by a previous filter. The material introduced in this section draws on many sources; the goal here is to present a compact formalism that permits us to compare the efficacy of these methods.

The following notation is used in the remainder of this paper. Let  $x_{if}(t) \in \mathbb{R}$  denote the energy from input spectrogram  $i$  at frequency index  $f$  for time sample  $t$  with  $i \in \{1, \dots, I\}$ ,  $f \in \{1, \dots, F\}$ , and  $t \in \{1, \dots, T\}$ .

We use  $\mathbf{x}_{if} = [x_{if}(1), x_{if}(2), \dots, x_{if}(T)]$  (written as a row vector) to specify the energy over time for frequency  $f$  in spectrogram  $i$ . The spectrum at time sample  $t$  from spectrogram

$i$  is denoted by the column vector

$$\mathbf{x}_i(t) = \begin{bmatrix} x_{i1}(t) \\ x_{i2}(t) \\ \vdots \\ x_{iF}(t) \end{bmatrix}.$$

$\mathbf{X}_i = [\mathbf{x}_i(1), \mathbf{x}_i(2), \dots, \mathbf{x}_i(T)]$  is the  $i$ -th spectrogram.

### 3.1. Time Centering, $\mathcal{T}$

Time centering refers to subtracting the mean of  $\mathbf{x}_i(t)$  from each of its elements. This basic operation removes fluctuations in total energy from one spectrum to the next. After centering, the (residual) energy in each spectrum sums to zero. Time centering the  $i$ -th spectrogram is defined as

$$\mathcal{T}\mathbf{X}_i \equiv (\mathbf{I}_F - \frac{1}{F}\mathbf{J}_F) \mathbf{X}_i$$

where  $\mathbf{I}_F$  is the identity matrix and  $\mathbf{J}_F$  is a square matrix of ones, both matrices having dimension  $F \times F$ . The operator notation,  $\mathcal{T}$ , mnemonically indicates a *time* centering filter.

### 3.2. Frequency Centering, $\mathcal{F}$

A frequency centering filter subtracts frequency means from a spectrogram, thus operating in the opposite direction of time centering. However, frequency centering is implemented on successive time windows of a spectrogram to limit the memory requirements for filtering a long stream of spectra. Let the  $n$ -th time window of the  $i$ -th spectrogram be

$$\mathbf{X}_{in} = [\mathbf{x}_i(nw - w + 1), \dots, \mathbf{x}_i(nw)].$$

where  $w$  is the number of time samples in the window. The  $i$ -th frequency-centered spectrogram is formed by removing frequency means from successive time windows:

$$\mathcal{F}\mathbf{X}_i \equiv [\mathbf{X}_{i1} (\mathbf{I}_w - \frac{1}{w}\mathbf{J}_w), \dots, \mathbf{X}_{iN} (\mathbf{I}_w - \frac{1}{w}\mathbf{J}_w)]$$

where  $N$  is the number of time windows in the spectrogram. This operation can be parallelized independently over the frequencies.

### 3.3. Energy Clipping, $\mathcal{C}$

Signals showing sudden spikes in the energies at all frequencies are likely to be terrestrial in origin. Time centering removes a uniform increase in energy at all frequencies. Energy clipping can ameliorate noisy spike that affect some frequencies more than others by truncating the  $L_2$  norm of a spectrum. This has the advantage of leaving the large majority of spectra unaltered; only spectra with unusually large  $L_2$  norm are modified.

Energy clipping of a spectrogram is defined as

$$\mathcal{C}\mathbf{X}_i \equiv [\phi(\mathbf{x}_i(1)), \phi(\mathbf{x}_i(2)), \dots, \phi(\mathbf{x}_i(T))]$$

where a clipped spectrum is given by

$$\phi(\mathbf{x}_i(t)) \equiv \begin{cases} \mathbf{x}_i(t), & \text{if } \|\mathbf{x}_i(t)\| < K \\ \frac{K\mathbf{x}_i(t)}{\|\mathbf{x}_i(t)\|}, & \text{otherwise.} \end{cases}$$

with  $\|\mathbf{x}_i(t)\| = [x_{i1}^2(t) + \dots + x_{iF}^2(t)]^{1/2}$ .

If the elements of  $\mathbf{X}_i$  are independent standard Gaussian variates, then  $\|\mathbf{x}_i(t)\|^2$  is a chi-squared random variable with  $F$  degrees of freedom. Setting  $K^2$  equal to an upper tail quantile of this distribution allows  $\mathcal{C}$  to pass the large majority of input vectors unchanged, truncating only a small fraction of nominally-generated vectors as well as any outlying vectors whose  $L_2$  norm is too large.

### 3.4. Huber Normalization, $\mathcal{H}$

Huber estimation is well-known in robust statistics (Huber 1964; Huber & Ronchetti 2009). The idea is to estimate a mean, variance, or other property of a distribution using thresholded versions of extreme values so that extreme values cannot unduly influence the estimates. The Huber calculations produce thresholded residuals on a normalized scale so residuals have mean approximately zero and standard deviation approximately one. These are called *winsorized residuals*. The recursive Huber filter described below produces winsorized residuals that are well-suited to detection of dispersed impulses because they are normalized and they mitigate RFI in individual energy values while retaining a substantial portion of an impulsive signal.



The Huber filter uses the Huber thresholding function at its core:

$$\psi(z) \equiv \begin{cases} -L, & \text{if } z < -L \\ z, & \text{if } -L \leq z \leq L \\ L, & \text{if } z > L \end{cases}$$

where the threshold  $L > 0$  must be specified. If  $z$  is a standard Gaussian random variable and  $L = 2$ , for example, then  $\psi(z) = z$  with probability about 0.95 and only the 5% most extreme values of  $z$  are truncated to  $\pm L$ .

For a generic sequence of real values  $\mathbf{y} = [y(1), y(2), \dots, y(T)]$ , the recursive Huber residuals, mean and variance are computed as

$$\begin{aligned} r(t) &= \psi\left(\frac{y(t) - m(t-1)}{s(t-1)}\right), \\ m(t) &= m(t-1) + ps(t-1)r(t), \\ s^2(t) &= (1-q)s^2(t-1) + (q/c)s^2(t-1)r^2(t), \end{aligned}$$

for  $t = 1, 2, \dots, T$ . We initialize the recursion with  $m(0) = y(1)$  and  $s^2(0) = 1$  and if  $s^2(t)$  becomes numerically zero, we arbitrarily reset it to 1. Only a long sequence of exactly constant input data would force a reset. The value of  $c$  is given below along with some discussion related to choice of tuning constants  $p, q \in (0, 1)$ .

The residual,  $r(t)$ , is formed by first standardizing the data value  $y(t)$  using mean and standard deviation estimates from the previous time period and then applying the  $\psi$  function to truncate to  $\pm L$ , if necessary. The mean estimate,  $m(t)$ , is modified from its previous value by a fraction  $p$  of the rescaled residual,  $s(t-1)r(t)$ . In the usual case with  $|r(t)| < L$ , the  $\psi$  function does nothing and thus  $s(t-1)r(t) = y(t) - m(t-1)$  and the mean update becomes  $m(t) = (1-p)m(t-1) + py(t)$ , a weighted average of the previous mean estimate and the new data value—the usual update formula for an exponentially weighted moving average (EWMA). The Huber mean estimate is thus an EWMA modified by truncation of large residuals. In a similar fashion, the variance is estimated as a weighted sum of the previous estimate and the new squared residual. The constant  $c$  is the expected value of  $\psi^2(z)$  with  $z$  being a standard Gaussian random variable, so that  $r^2(t)/c$  has expectation near unity, making  $s^2(t)$  nearly unbiased. Based on the variance of a truncated Gaussian distribution (e.g., Johnson et al. 1994, section 10.1), we obtain

$$c = 1 - 2[L\phi(L) - (L^2 - 1)\Phi(-L)],$$

where  $\phi$  and  $\Phi$  are the standard Gaussian density and cumulative probability functions.

Choices for  $p, q \in (0, 1)$  can be made by noting that the EWMA corresponding to the Huber filter gives weight  $p(1-p)^i$  to the lagged observation  $y(t-1-i)$ . This exponentially decreasing sequence of weights has effective window width  $(2-p)/p$  so that an effective window width of  $n$  samples is obtained by taking  $p = q = 2/(n+1)$ , and this holds approximately for the Huber analog of the EWMA.

We define winsorized residuals produced by Huber filtering of a sequence  $\mathbf{y}$  and a spectrogram  $\mathbf{X}_i$  as

$$\mathcal{H}\mathbf{y} \equiv [r(1), r(2), \dots, r(T)]$$

and

$$\mathcal{H}\mathbf{X}_i \equiv \begin{bmatrix} \mathcal{H}\mathbf{x}_{i1} \\ \mathcal{H}\mathbf{x}_{i2} \\ \vdots \\ \mathcal{H}\mathbf{x}_{iF} \end{bmatrix}$$

respectively. The Huber filter operates independently over all frequencies in parallel.

### 3.5. Adaptive Interference Cancellation, $\mathcal{A}$

Barnbaum & Bradley (1998) achieved attenuation of 72 dB in the first AIC system used in the radio astronomy domain. The value of using more than one reference antenna was also made explicit: it permits cancellation of a greater number of uncorrelated noise sources. We use the primary idea of AIC—subtracting interference identified by correlating with reference antennas—but adapt it to the fast spectrum data collected by ATA in Fly’s Eye mode. The major difference from typical applications is that phase information is not available in the ATA energy spectra. Even so, interference can be estimated by dynamic linear combinations of the primary and reference spectra. Subtracting estimated interference from the primary spectra mitigates its impact on dispersed pulse detection.

AIC assumes that a primary sensor receives a signal of interest plus interference that is not correlated with the signal. In addition, some number of reference sensors do not receive the signal of interest but do receive the same interference as the primary sensor plus noise that is uncorrelated with the interference. These are reasonable assumptions for Fly’s Eye data because individual antennas are sensitive to astronomical signals originating in different regions of the sky and both atmospheric and terrestrial RFI typically infect multiple antennas.

An important quality of AIC is that it makes very few assumptions about the characteristics of the interference. AIC can be used to mitigate a wide class of RFI that appears

simultaneously in multiple antennas. If a specific RFI pattern is prevalent (e.g., the 60 Hz signals common in radio astronomy observations), then an effective RFI filter can be designed to mitigate that specific type of signal. AIC is likely to be somewhat less efficient at mitigating specific known interference patterns, but AIC is adaptive in the sense that it will handle a wide class of interferers without the need to design a different filter for each type of interference.

The AIC filter on a spectrogram is defined on successive windows of an input sequence  $\mathbf{x}_{if}$ . Let the  $n$ -th window of  $\mathbf{x}_{if}$  be

$$\mathbf{x}_{ifn} = [x_{if}((n-1)w+1), \dots, x_{if}(nw)].$$

AIC is first applied to  $\mathbf{x}_{if1}$ , then to  $\mathbf{x}_{if2}$ , and so on.

To filter the  $n$ -th window, create a matrix,  $\mathbf{A}_{ifn}$ , with rows being the windowed signals for frequency  $f$  from each of the reference spectrograms,  $\mathbf{x}_{kfn}$ ,  $k \in \mathbb{K}_i \subseteq \{1, \dots, i-1, i+1, \dots, I\}$ . For example, if the reference set for cleaning  $\mathbf{x}_{1fn}$  is  $\mathbb{K}_1 = \{2, \dots, I\}$  (i.e., all other signals), then

$$\mathbf{A}_{1fn} = \begin{bmatrix} \mathbf{x}_{2fn} \\ \mathbf{x}_{3fn} \\ \vdots \\ \mathbf{x}_{Ifn} \\ \mathbf{1}'_w \end{bmatrix}$$

where  $\mathbf{1}_w$  is a vector of  $w$  ones and is included in every  $\mathbf{A}_{ifn}$  matrix.

AIC cleans the signal  $\mathbf{x}_{ifn}$  by subtracting its linear projection on  $\mathbf{A}_{ifn}$  to obtain residuals

$$\mathbf{e}_{ifn} \equiv \mathbf{x}_{ifn}(\mathbf{I}_w - \mathbf{A}'_{ifn}(\mathbf{A}_{ifn}\mathbf{A}'_{ifn})^{-1}\mathbf{A}_{ifn})$$

where  $\mathbf{I}_w$  is the identity matrix of dimension  $w$ . For a signal  $\mathbf{x}_{if}$  consisting of  $N+1$  windows, AIC cleaning is denoted by

$$\mathcal{A}\mathbf{x}_{if} = [\mathbf{e}_{if0}, \dots, \mathbf{e}_{ifN}]$$

and parallel cleaning of each frequency in a fast spectrogram is denoted by

$$\mathcal{A}\mathbf{X}_i \equiv \begin{bmatrix} \mathcal{A}\mathbf{x}_{i1} \\ \mathcal{A}\mathbf{x}_{i2} \\ \vdots \\ \mathcal{A}\mathbf{x}_{iF} \end{bmatrix}.$$

In an antenna array, different antennas will have different frequency response curves and will receive different RFI signals due to differences in direction of arrival, local terrain, and

so forth. The AIC formulation is effective, however, even when the intensity of RFI varies by antenna and by frequency because the projection onto  $\mathbf{A}_{ifn}$  is the best (least-squares) linear combination of the reference windows for estimating the RFI in the target input sequence  $\mathbf{x}_{ifn}$ .

The algorithm requires specification of the window width  $w$  and the set of reference signals. We set  $w = 640$  samples, which, at the sampling rate of 1600 Hz, is about 400 ms. Choice of reference signals is discussed in Section 5.

Note that for the Fly’s Eye data we are operating on power spectra rather than time-series voltage data, which is the conventional target. Nevertheless, the projection method described here applies to both and can be used to remove RFI.

#### 4. Chirp Detection

Examples of chirped signals from the Crab pulsar appear in Figure 1. The presence of a chirp is indicated by higher than expected values of energy in the pixels along the *chirp path*. We define the chirp path with time index  $t$  and dispersion measure DM as

$$\mathbb{C}(t, \text{DM}) = \{(f, \tilde{t}) : \text{the center of pixel } (f, \tilde{t}) \text{ is bracketed by chirps that begin at } t \pm 0.5 \text{ with dispersion measure DM}\}.$$

This is illustrated in Figure 3 for  $t = 3$  and a specific dispersion measure. The black curves are chirps starting at  $t \pm 0.5$  with dispersion delay given by the cold plasma dispersion law. The grid of dashed lines indicates pixel boundaries in a spectrogram. If the center of a pixel lies between the chirps then it is in the chirp path for the given start time ( $t$ ) and dispersion measure (DM).

While there are many other ways that a discrete chirp path could be defined, this definition has the desirable quality that every pixel in the spectrogram belongs to one and only one chirp path for a given dispersion measure. Therefore, successive chirp paths do not share pixels and so are statistically independent of each other as long as the energy values at different pixels are independent of each other.

##### 4.1. Sequence of T-tests

Our approach to determining whether a chirp is present along a chirp path is to perform a standard t-test comparing the mean energy for pixels in the chirp path to the mean for

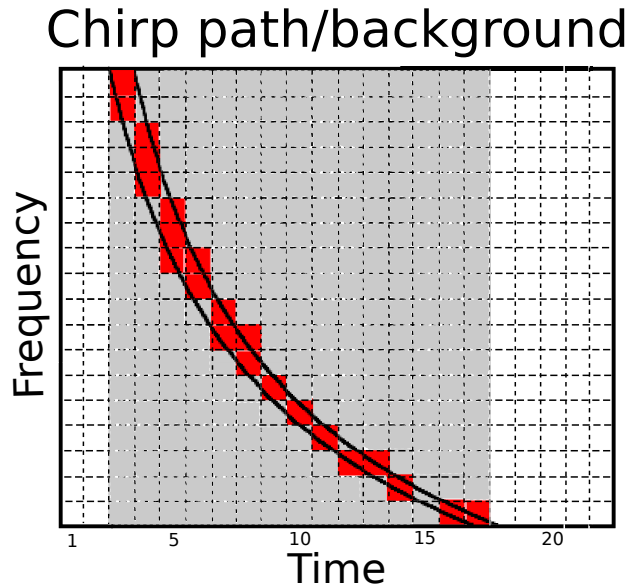


Fig. 3.— The chirp path for a chirp starting at time 3 is shown by the red pixels. The two bold curves illustrate chirps with the same dispersion measure. One chirp starts at the beginning of time sample 3 and the second chirp starts at the end of time sample 3. The pixels in the chirp path are those pixels with centers between the two continuous chirps.

pixels in the background. The set of background pixels for a chirp starting at time  $t$  with dispersion measure DM is denoted as  $\bar{\mathbb{C}}(t, \text{DM})$  and consists of pixels concurrent with the chirp path but excluding the chirp path, as indicated by gray shading in Figure 3.

The t-test and the effects of deviations from its sampling assumptions are discussed in many introductory statistics tests (e.g., Glass & Hopkins 1996). The Gaussian assumption becomes less important with larger samples. Non-constant means and variances in the chirp path or the background have the potential to affect both the false alarm rate of the test statistic and its ability to make correct detections.

A large t-score indicates the presence of a chirp. If the pixels in  $\mathbb{C}(t, \text{DM})$  and  $\bar{\mathbb{C}}(t, \text{DM})$  are independent and identically distributed (iid) samples drawn from Gaussian distributions, then the t-scores are drawn from a t-distribution with  $n_b + n_c - 2$  degrees of freedom.

In this paper we only explore analysis of pulses with a width equal to the sampling

time. Real astronomical pulses, however, can have widths much larger than the sampling time. These broader pulses can be addressed through hierarchical averaging of the time series data and application of the same chirp integration.

## 5. Tests on Synthetic Chirps

We tested various combinations of the RFI mitigation filters described in Section 3 on ATA data in Fly’s Eye mode. Specifically, one hour of power spectrograms was extracted simultaneously from 44 receivers with 128 frequency channels from  $\nu_1 = 1325$  MHz to  $\nu_F = 1535$  MHz, with a frequency resolution of  $\Delta f = 1.64$  MHz per channel. (Although the ATA has 42 antennas, each has a dual linear polarization feed, making 84 independent signal streams. Our hardware captures 44 of these signals, and we refer to them as antennas to simplify exposition.)

Figure 4 shows a “Rogues Gallery” of 10 spectrogram segments containing different amounts and types of unwanted signal. These are some of the worst cases. The vast majority of data segments would appear as white noise in this type of display. Each spectrogram in Figure 4 also has an artificially embedded chirp that is visible beginning at 100 ms in the highest frequency of each segment and sweeping through the frequency band over about 35 ms of time. These 10 segments include impulsive RFI, such as the white vertical lines in (H) and (I), as well as single-frequency transients, such as the horizontal streaks at about 1375 MHz in (B) and (J). The black and white bands in (A) alternate at 60 cycles per second, which is likely an instrumentation artifact, along with the similar but subtler patterns in (B), (D) and (E). We refer to all of this clutter as RFI, even though some of it is not likely to have originated in the radio frequency domain.

The artificial chirps in Figure 4 have a  $DM = 57\text{pc}/\text{cm}^3$  corresponding to that of the Crab pulsar. To embed a chirp starting at a particular time, we added energy to appropriate frequency bins in each spectrogram during the duration of the chirp. We use the cold plasma dispersion law to find the chirp frequency for each time sample from the start of the chirp to the end of the chirp. For each time sample during a chirp, energy was typically added to two frequency bins – the two bins bordering the chirp frequency—with the total energy  $E_0$  split in proportion to the distances between the bin frequencies and the chirp frequency. For example, if the embedded chirp has frequency  $\nu_c$  and the bordering bins have center frequencies  $\nu_L$  and  $\nu_H = \nu_L + \text{Delta}$ , then energy  $E_0 - E_0(\nu_c - \nu_L)/\Delta$  is added to the bin with frequency  $\nu_L$  and the remainder is added to the next higher bin.

The examples in Figure 4 show embedded chirps with energy level  $E_0 = 2.0$ . This is

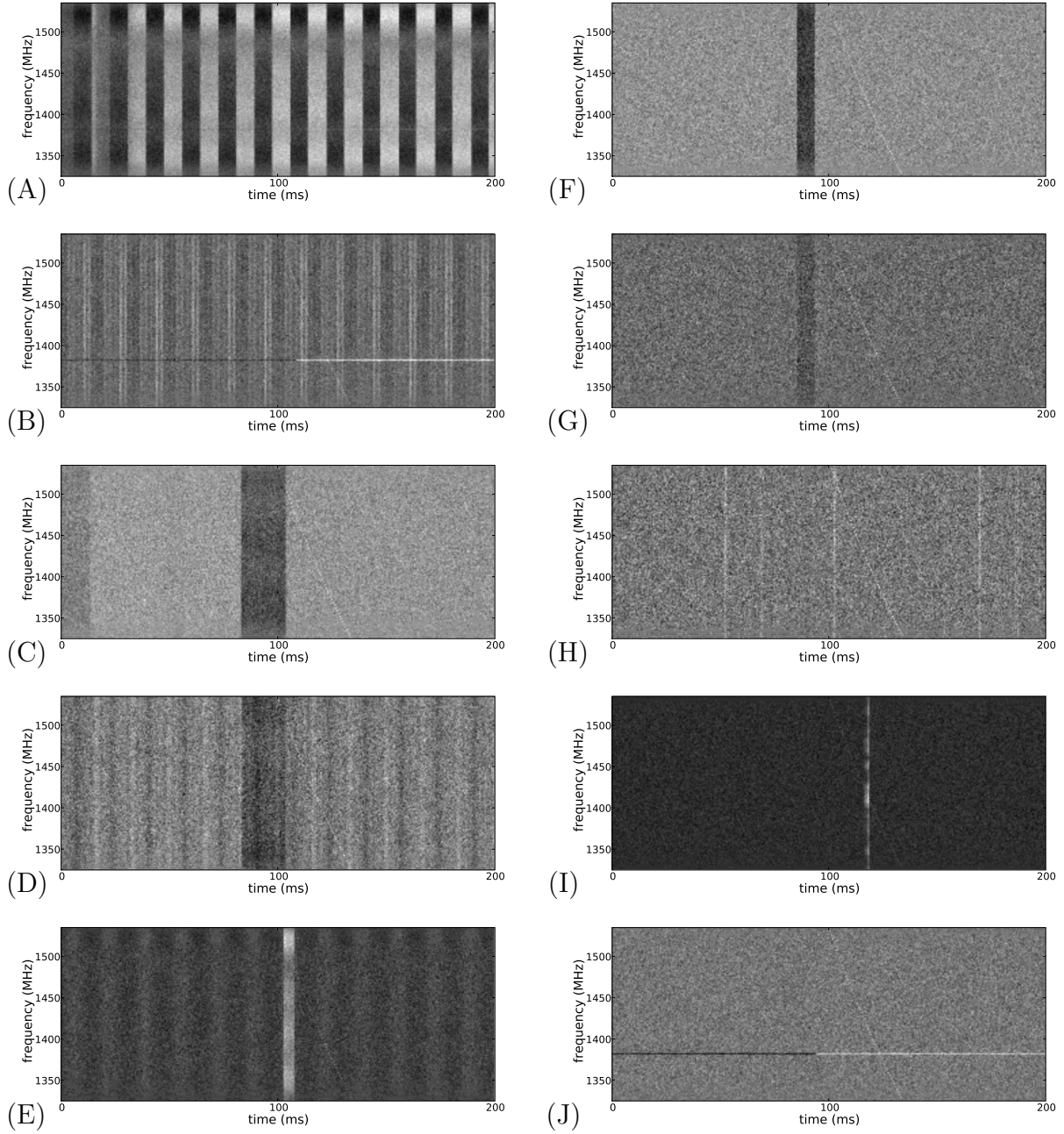


Fig. 4.— Ten examples of RFI, (A)–(J), with chirps embedded beginning at 100 ms at an energy level of 2.0.

the strongest of four energy levels used for this study: 0.75, 1.0, 1.25 and 2.0. (Although measurements in our spectrograms are proportional to energy, at the time these data were collected the ATA Fly’s Eye mode did not calibrate each antenna to an absolute reference. Therefore, embedding chirps with fixed energy  $E_0$  into uncalibrated data equates to embedding signals of differing absolute strength, depending on the antenna gain.) Figure 5 shows the RFI in panel (G) from Figure 4 with the chirp embedded at the strongest ( $E_0 = 2.0$ , top) and weakest ( $E_0 = 0.75$ , bottom) energy levels. The weak chirp is barely visible in the lower image but was detected at a level as low as 5 false alarms in 138 million time samples, equivalent to one full day of observing.

Figure 6 illustrates the process we used to compare the effectiveness with which various filtering strategies (discussed further below) mitigate RFI. Each of the 44 antenna output files used for our study is approximately an hour in length. Seven of these files were used to provide examples of RFI. In three of the seven files, we studied RFI at two different times, and in the remaining four, we chose only a single time, making total of 10 different RFI exemplars as shown in Figure 4.

Chirps were embedded with each of the four energy levels listed above in each of the 10 exemplars for a total of 40 examples of embedded chirps. The data set with embedded chirps is referred to as the *test set*.

Another 17 of the 44 files were randomly selected, so that together with the seven files in the test set, a total of 24 files are identified as the *reference set*. The reference set represents approximately 24 hours worth of data. The reference set was processed identically to the test set and used to determine how many false alarms to expect per day for thresholds corresponding to detection of each of the 40 different embedded signals.

From the remaining 20 files (those not used in the reference set), 10 were randomly chosen as the cleaning signals to use with AIC filtering. The remaining 10 files were not used in the tests reported here.

Each filtering strategy aimed at mitigating RFI was applied to both the test set and the reference set, followed by t-test calculations for chirp detection. The number of t-scores in the reference set greater than or equal to the t-score for each embedded chirp in the test set is the number of false alarms. False alarm counts were computed for each combination of four energy levels and the 10 RFI sections in the reference set, giving 40 false alarms counts for a given filtering strategy.

Six filtering strategies were tested using the processing described above and illustrated in



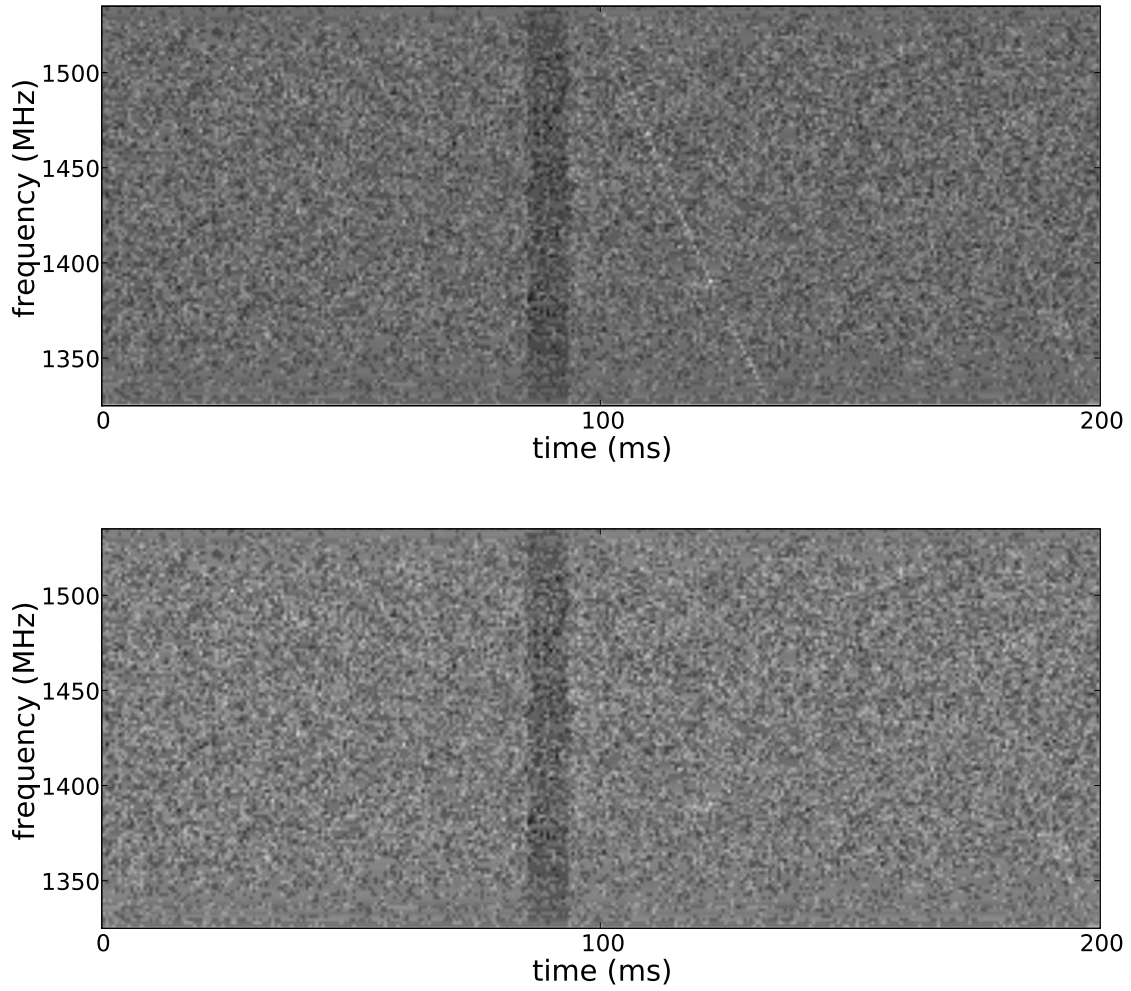


Fig. 5.— Strongest ( $E_0 = 2.0$ ) and weakest ( $E_0 = 0.75$ ) embedded energy on the (J) section of RFI.

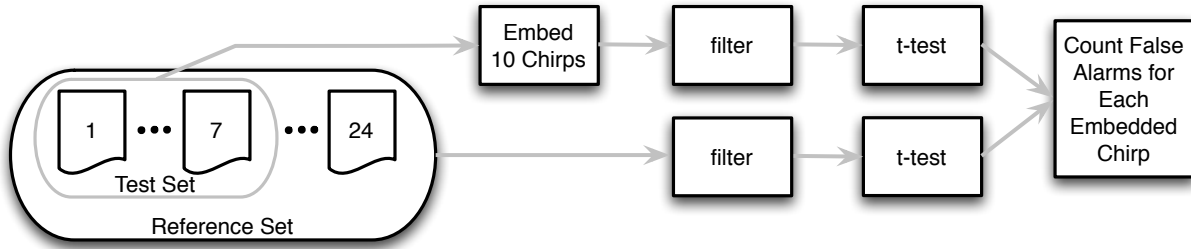


Fig. 6.— Process of testing a detection method on synthetic chirps. The figure illustrates the processing that was done for a given embedded signal strength,  $E_0$ , and a given RFI filter. This was repeated for each combination of four signal strengths and six filters.

Figure 6. Each filtering strategy consists of a combination of the mitigation filters presented in Section 3. The six strategies, identified by short names, are defined below and rationale is given for the specific choices selected for each strategy. Frequency centering and AIC filters operate on consecutive time windows of spectrograms. In each case below, the window size was set to  $w = 640$  samples, corresponding to 400 ms time windows. This window size is about 11 times longer than the embedded chirps so that the chirp represents only a small fraction of data in a window.

The filtering strategies are as follows:

**none:** is the t-test detector on the raw spectrograms—no filter is applied. This is included for reference, even though it is not a competitive strategy.

**center freq:** is frequency centering in which frequency means are subtracted from successive spectrogram windows. This filter is included primarily for a comparison with the following strategy.

**center freq + AIC:** applies frequency centering to the file to be cleaned and to each of the 10 AIC cleaning files. Then AIC is run on each window of the spectrogram. Comparing this strategy to the previous one allows for measuring the value of the more complex AIC calculations beyond the simple frequency centering calculations. If no reference signals were used in the AIC cleaning algorithm, AIC would be identical to the "center freq" approach above. To emphasize that AIC centers the frequencies *and* uses additional reference signals, we write "center freq + AIC" for the case where frequency centering is applied to the file to be cleaned and to each of the 10 AIC cleaning files before applying AIC.

**center freq,time:** performs frequency centering (in windows) and then time centering. This allows for comparing the value of time centering beyond that of frequency centering (the second strategy) and provides a reference for the following strategy.

**center freq,time + AIC:** is frequency and time centering (as above) on the file to be cleaned and on each file in the AIC cleaning set. Then AIC is run on each window of the spectrogram. Comparison to the previous strategy shows the incremental value of AIC beyond two-way centering.

**Huber + center time + energy truncation:** first applies Huber filtering with  $p = q = 0.001249$ , and  $L = 2$ . Next the mean energy at each time is removed. Finally the energy clipping filter is applied with a threshold of  $K = 155$ . This strategy is intended to determine the value of outlier mitigation as implemented in Huber filtering and energy clipping. Choices of  $p$  and  $q$  come from setting the effective window width to 1600 samples ( $p = q = 2/1601$ ), so that the smoothing is scaled to one second of time. This is much longer than the 400 ms used for AIC and frequency centering. The rationale is that the combination of Huber filtering and energy clipping mitigates outlying RFI data values so that smoothing can be done on longer time scales without the risk of bad data corrupting the filter output for a prolonged period. The value  $L = 2$  should clip approximately 5% of the individual data values in the Huber thresholding function. Similarly  $K = 155$  is the 0.95 quantile of the  $\chi^2$  distribution with  $F = 128$  degrees of freedom and this should clip energy from approximately 5% of the normalized spectra as explained in Section 3.3. These are reasonable choices informed by usual practices in application of robust statistics.

## 6. Results & Discussion

### 6.1. Detection Sensitivity and False Alarm Rates

A good measure of the ability of a filter combination to mitigate RFI and retain the signal of a chirp is the count of t-scores greater than or equal to the t-score of a given chirp. For example, after embedding a chirp in one of the test-set files and running a given filter combination over the data, suppose the chirp generates a t-score of  $t_0$ . The number of false alarms for this case is determined by counting how many t-scores are greater than  $t_0$  when the same filtering is applied to the 24 hour reference set with no embedded chirps. False detection counts are obtained for each embedded chirp in combination with each choice of RFI filter.

Figure 7 plots false detections in 24 hours corresponding to each of the 10 RFI examples

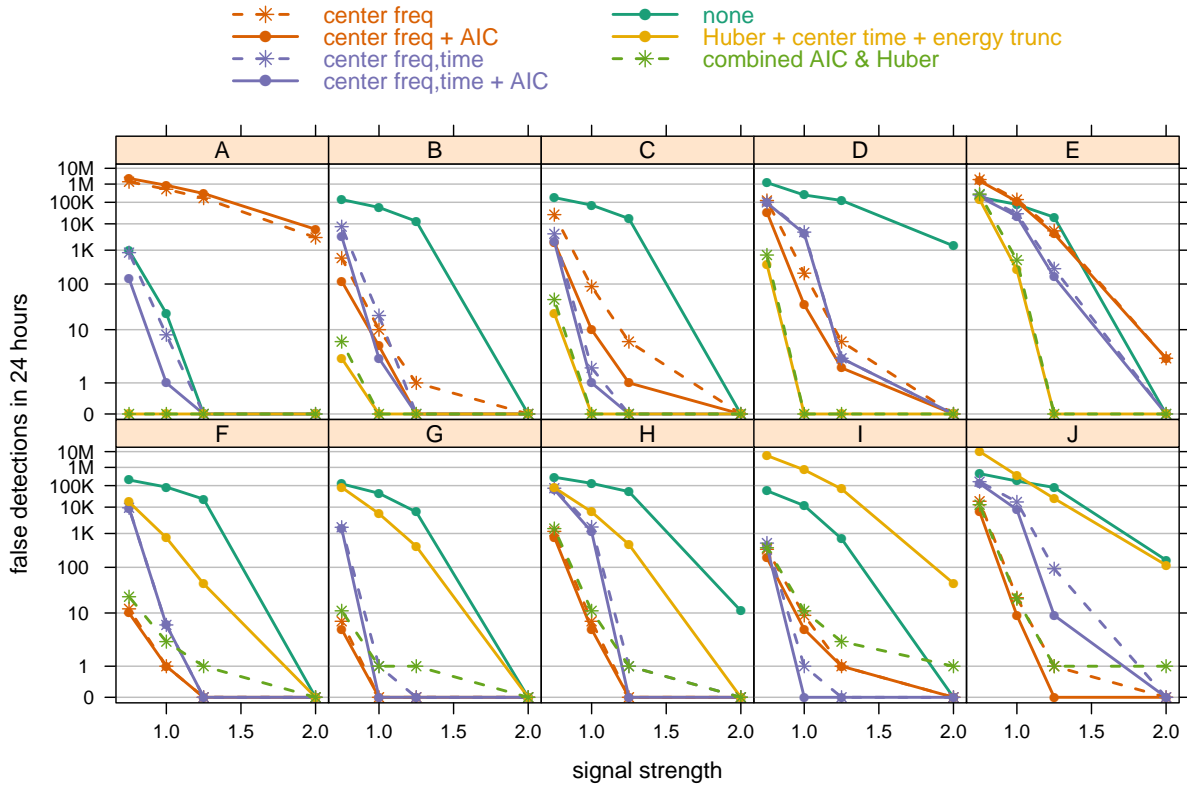


Fig. 7.— False alarm counts on 10 embedded chirps using six combinations of RFI mitigation filters.

shown in Figure 4 with various strengths of embedded chirps and various combinations of filtering. Within each panel, different lines correspond to different filter combinations and each line presents false detections for each of five embedded chirp strengths. Six of the seven lines are for the six filter combinations detailed in Section 5. The seventh, labeled “AIC & Huber,” is discussed below. False detection counts drop toward zero as the strength of the embedded signal increases. The vertical axis is scaled to emphasize the low range of false detections. Values above 100 represent chirps that could not reasonably be detected by close individual analysis of all detections in a single day of observation time.

The RFI examples, A–J, in Figure 4 and the corresponding panels in Figure 7 are ordered according to decreasing success of the Huber filter, center time, and energy clipping combination. Interestingly, centering filters with and without AIC tend to perform well when Huber does poorly, and vice versa. In particular, in the top row of plots, the Huber filter

is uniformly best, while it is not much better than no filtering in the bottom row of plots. However, the “center freq. + AIC” filter is best in the bottom row of plots, except for case “I” where the two frequency and time centering filters do somewhat better.

The fact that the Huber filter complements “center freq. + AIC” suggests that a better strategy would be to combine both methods, as described below. In fact, the lines labeled “combined AIC & Huber” show that the combined AIC and Huber method does indeed perform well on all ten embedded chirps. The combined method is not uniformly best, but it is the only strategy that never performs poorly relative to the other filters.

False alarms for the “combined AIC & Huber” strategy were computed as follows. Let  $C$  denote the minimum of the false detection counts for “center freq. + AIC” and for “Huber + center time + energy truncation”. This  $C$ -score is computable from the empirical distribution of  $t$ -scores over the 24 hour reference set and is itself a detection statistic. A small  $C$ -score near zero denotes strong evidence of a chirp. For an embedded chirp with  $C = c_a$ , the false detection count is the number of  $C$ -scores in the reference set that are less than or equal to  $c_a$ . These counts are shown in Figure 7 for the “combined AIC & Huber” method.

## 7. Summary and Conclusions

Radio frequency interference is a dominant limiting factor in the design and performance of fast radio transient experiments. We present here an analysis of the effectiveness of several RFI mitigation methods, with the goal of a more rigorous statistical understanding of the performance of these filters. We apply these methods to actual interference present in data obtained as part of the ATA Fly’s Eye survey. A search for synthetic dispersed pulses that were added to the interference data was employed as a means to determine the rate of false detections. Filters explored in various combinations include time centering, frequency centering, adaptive interference cancellation (AIC), Huber filtering, and energy clipping.

Huber filtering in combination with energy clipping and time centering proved very effective at eliminating RFI that was primarily broad in frequency but variable in time. In many cases, application of these filters led to zero false positives when applied to 24 hours of data. For the case of RFI that is predominantly frequency-dependent, the Huber filter is largely ineffective. In these cases, frequency centering with and without AIC is the most effective. Unfortunately, the frequency centering approach produces many false positives for broadband RFI. A method that combines Huber and AIC filtering proves uniformly effective over a range of time- and frequency-dependent interferers. It is the only method explored

that will produce a low number of false positives under all RFI examples considered here.

AIC is computationally intensive and is applicable to only the subset of experiments in which reference signals are available. The computational complexity of AIC is much higher than that for using a robust filtering approach. For example, given signals from  $N$  antennas, each having  $F$  frequency channels output at each time, we will need to use AIC on  $NF$  primary signals with up to  $N - 1$  reference signals for each primary signal. This implies that we need to form and solve  $NF$  systems of linear equations for each primary signal in each window of time. If we use the maximum number of reference signals, then the algorithm does not scale well with increasing numbers of radio antennas. While modern computing devices are often optimized to do linear algebraic calculations as needed for AIC, as the number of antennas grows, the computational burden may eventually be too high.

To decrease the computational costs, compromises will need to be made. For example, we may have to arrange radio telescopes so that telescopes that are close to each other point to different locations in space. This will help ensure that the same noise signals are observed by each telescope but the signals of interest will not be observed by multiple telescopes. Doing this will allow fewer reference signals to be used for each primary signal. Alternately, AIC could be used as a second stage of processing to further clean spectra that are suspected of having dispersed impulses. We need to understand the trade-offs of various AIC algorithms, and how the AIC algorithms interact with other RFI mitigation techniques as well as pulse detection techniques.

Finally, we note that the forms of RFI used for testing these algorithms are by no means exhaustive. It is certainly of interest to apply these algorithms to data obtained from other telescopes in different RFI environments. Nevertheless, we see promise in Huber filtering and AIC for mitigation of RFI from incoherent spectra in the search for fast radio transients.

The authors would like to acknowledge the generous support of the Paul G. Allen Family Foundation, who have provided major support for design, construction, and operations of the ATA. Contributions from Nathan Myhrvold, Xilinx Corporation, Sun Microsystems, and other private donors have been instrumental in supporting the ATA. The ATA has been supported by contributions from the US Naval Observatory in addition to National Science Foundation grants AST-050690 and AST-0838268. This work received funding from Los Alamos National Laboratory LDRD Project #20080729DR. We thank Griffin Foster and Peter McMahon for their contributions to the Fly’s Eye experiment.

## REFERENCES

- Baan, W. 2010, in RFI Mitigation Workshop: Published online at <http://pos.sissa.it/cgi-bin/reader/conf.cgi?confid=107>
- Barnbaum, C., & Bradley, R. F. 1998, *AJ*, 116, 2598
- Bhat, N. D. R., Tingay, S. J., & Knight, H. S. 2008, *ApJ*, 676, 1200
- Bower, G. C. 2001, *ATA Memo Series*, 31
- Bower, G. C. 2005, *Radio Science*, 40, RS5S07
- Burke-Spolaor, S., Bailes, M., Ekers, R., Macquart, J.-P., & Crawford, III, F. 2011, *ApJ*, 727, 18
- Cordes, J., Lazio, T., & McLaughlin, M. 2004, *New Astronomy Reviews*, 48, 1459
- Cordes, J. M., Bhat, N. D. R., Hankins, T. H., McLaughlin, M. A., & Kern, J. 2004, *AJ*, 612, 375
- Deneva, J. S., Cordes, J. M., McLaughlin, M. A., et al. 2009, *ApJ*, 703, 2259
- Ellingson, S. W. 2005, *Radio Science*, 40, RS5S01
- Ellingson, S. W., & Hampson, G. A. 2003, *ApJS*, 147, 167
- Glass, G. V., & Hopkins, K. D. 1996, *Statistical methods in education and psychology* (Allyn & Bacon), 444–480
- Hankins, T. H., Kern, J. S., Weatherall, J. C., & Eilek, J. A. 2003, *Nature*, 422, 141
- Huber, P. 1964, *The Annals of Mathematical Statistics*, 35, 73
- Huber, P., & Ronchetti, E. 2009, *Robust statistics* (John Wiley & Sons Inc)
- Johnson, N., Kotz, S., & Balakrishnan, N. 1994, *Continuous Univariate Distributions, Volume 1* (New York: John Wiley & Sons)
- Keane, E. F., Kramer, M., Lyne, A. G., Stappers, B. W., & McLaughlin, M. A. 2011, *MNRAS*, 415, 3065
- Kesteven, M., Hobbs, G., Clement, R., et al. 2005, *Radio Science*, 40, RS5S06
- Kocz, J., Briggs, F., & Reynolds, J. 2010, *AJ*, 140, 2086

- Kramer, M., & Stairs, I. H. 2008, *ARA&A*, 46, 541
- Leshem, A., van der Veen, A., & Boonstra, A. 2000, *ApJS*, 131, 355
- Li, S.-Y., Ali, E., & Sun, Z.-W. 2008, in *Image and Signal Processing, 2008. CISP '08. Congress on*, Vol. 4, 469–472
- Lorimer, D., Bailes, M., McLaughlin, M., Narkevic, D., & Crawford, F. 2007, *Science*, 318, 777
- Macquart, J., Bailes, M., Bhat, N. D. R., et al. 2010, *PASA*, 27, 272
- McLaughlin, M., Lyne, A., Lorimer, D., et al. 2006, *Nature*, 439, 817
- Nita, G. M., & Gary, D. E. 2010, *MNRAS*, 406, L60
- Ransom, S. M. 2001, in *Bulletin of the American Astronomical Society*, Vol. 33, American Astronomical Society Meeting Abstracts, #119.03–+
- Siemion, A., Von Korff, J., McMahon, P., et al. 2010, *Acta Astronautica*, 67, 1342
- Siemion, A., Bower, G. C., Foster, G., et al. 2011, *ApJ*, submitted
- Weber, R., Faye, C., Biraud, F., & Dansou, J. 1997, *A&AS*, 126, 161
- Welch, J., Backer, D., Blitz, L., et al. 2009, *Proceedings of the IEEE*, 97, 1438
- Widrow, B., & Stearns, S. 1985, *Adaptative signal processing* (Prentice-Hall)